

# Dynamic Connectivity without Sliding Windows

Shih-Gu Huang, Moo K. Chung, Ian C. Carroll, and H. Hill Goldsmith

**Abstract—Objective:** Sliding and tapered sliding window methods are the most often used approaches in computing dynamic correlations in biomedical signals such as the brain resting-state fMRI. However, due to the discrete nature of windows, the window methods suffer spurious high-frequency fluctuations and the zig-zag pattern in dynamic correlations. **Methods:** To address the problem and obtain more stable correlation estimates, we propose a novel windowless approach for computing dynamic correlations via heat kernel smoothing. The heat kernel, the natural generalization of the Gaussian kernel to manifolds, is used to defined a smoothing kernel without boundary or end points. **Results:** We show that the proposed windowless approach smooths out the unwanted high-frequency noise in correlation estimations and is more stable in identifying and discriminating state spaces in resting-state fMRI. The proposed method is applied to the study of interhemispheric connectivity and whole-brain network analysis. **Conclusion:** We present a novel framework using heat kernel to compute the windowless dynamic correlation, which is more stable with less high-frequency fluctuations than windowed methods. **Significance:** The proposed windowless approach reduced the spurious rapid changes in the state space of brain connectivity, and identified the strongest connections in brain networks and symmetry in interhemispheric connectivity.

**Index Terms**—Dynamic functional connectivity, windowless dynamic correlation, heat kernel smoothing, sliding windows, resting state fMRI

## I. INTRODUCTION

Findings of resting-state fMRI have revealed synchrony between spontaneous blood-oxygen-level-dependent (BOLD) signal fluctuations in sets of distributed brain regions despite the absence of any explicit tasks [1]–[4]. The time-invariant static measures of functional connectivity are often computed over the entire scan duration. However, this oversimplification reduces the complex dynamics of the resting-state functional connectivity to the time average. Recent studies have suggested the dynamic changes in functional connectivity over time even during rest, referred to as the *dynamic functional connectivity* [1]–[4].

The most common approach to modeling dynamic connectivity is through the sliding windows, where dynamic correlations are computed over the consecutive windowed segments of fMRI time series data over predefined brain parcellation [3], [5]–[11]. The sliding window (SW) method using a square window [2], [3], [5]–[10] is the most commonly

This study was supported by NIH research grants EB022856, MH101504, P30HD003352, U54HD09025 and UL1TR002373. (Corresponding author: Moo K. Chung.)

S.-G. Huang is with the Department of Biostatistics and Medical Informatics, University of Wisconsin, Madison, WI, USA.

M. K. Chung is with the Department of Biostatistics and Medical Informatics & Waisman Laboratory for Brain Imaging and Behavior, University of Wisconsin, Madison, WI, USA (e-mail: mkchung@wisc.edu).

I. C. Carroll and H. H. Goldsmith are with the Waisman Center & Department of Psychology, University of Wisconsin, Madison, WI, USA.

used windowed methods. To remedy the zig-zag pattern in the SW-method caused by the use of square window, the tapered sliding window (TSW) using a square window convolved with a Gaussian kernel [7], [12], [13], Hamming window [14], Tukey window [15] and exponentially decaying window [12] methods were proposed. However, the sidelobes of the window functions in spectral domain will cause high-frequency fluctuations in the dynamic correlations in all these methods [16]. To address the problem caused by using a window function with a finite support, we propose to use a kernel function without endpoint or boundary in computing dynamic correlation over the whole domain of the data, referred to as the *windowless dynamic correlation* in this paper. By solving heat diffusion on a circle, the heat kernel, the most natural generalization of the Gaussian kernel, can be derived on the circle continuously without boundary and can be represented in terms of the cosine basis functions. The windowless dynamic correlations using heat kernel are then computed by the weighted cosine series expansion, where the weights are related by the heat kernel [17]. We show that the proposed windowless method smooths out unwanted high-frequency noises in dynamic correlation estimation.

One can summarize the whole-brain dynamic functional connectivity time courses into a smaller set of *dynamic connectivity states*, defined as distinct transient connectivity patterns that repetitively occur throughout the resting-state scan [3]. They are reliably observed across different subjects, groups and sessions [18], [19]. *k*-means clustering on resting-state fMRI was introduced in [7] and subsequently adopted by many others [3], [20]–[23] to identify these recurring dynamic functional connectivity states that are common across subjects. It has been shown that additional summary metrics of the fluctuations in these clustering-derived states, such as the amount of time spent in specific states and the transition between states, exhibit meaningful between-group variations such as age [3], [24] and clinical status [20], [22], [25], [26]. We show that the proposed windowless method is more stable than the SW- and TSW-methods in identifying and discriminating states while reducing within state variability.

The main outline and main contributions of the paper are the followings. 1) We present a novel framework to compute the windowless dynamic correlations using heat kernel. 2) The proposed windowless method is applied in identifying and discriminating the state spaces in the dynamic interhemispheric connectivity and dynamic whole brain connectivity in the resting-state fMRI of 479 healthy subjects.

## II. PRELIMINARY

We give a brief review widely used methods of windowed dynamic correlation, which will be compared to the proposed

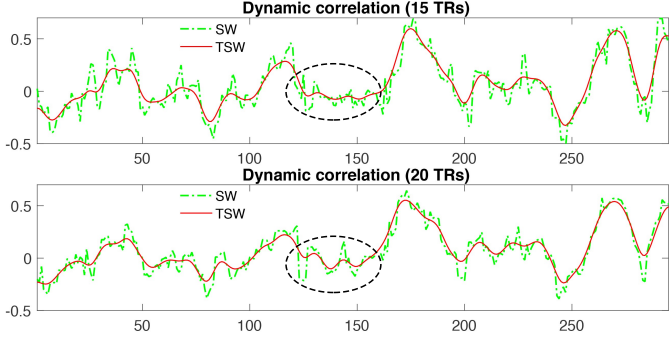


Fig. 1. Dynamic correlations computed by the SW- and TSW-methods with window size measured as the full width at half maximum (FWHM) 15 (top) and 20 (bottom) TRs. The SW-method shows the zig-zag severe pattern. The TSW-method reduced the zig-zag pattern but we can still observe high frequency fluctuations. These zig-zag pattern and high-frequency fluctuations were not eliminated and became even worse in some intervals (dashed circles) when larger window size was used indicating they are in fact artifacts produced by the use of discrete windows.

windowless dynamic correlation method through the paper.

*Sliding window method.* Consider time series  $\mathbf{x} = (x_0, x_1, \dots, x_{T-1})$  and  $\mathbf{y} = (y_0, y_1, \dots, y_{T-1})$  with  $T$  data points. To avoid the boundary effect in windowed methods [27], we connect the data at the end points by their mirror reflection and make them into the circular data with  $2T$  data points:

$$\begin{aligned}\mathbf{x} &= (\dots, x_2, x_1, x_0, x_1, x_2, \dots, x_{T-1}, x_{T-1}, x_{T-2}, \dots), \\ \mathbf{y} &= (\dots, y_2, y_1, y_0, y_1, y_2, \dots, y_{T-1}, y_{T-1}, y_{T-2}, \dots).\end{aligned}$$

Let  $W_m(i) = [i - \frac{m}{2} + 1, i + \frac{m}{2}]$  be the sliding window of size  $m$  at time point  $i$ . The sliding window (SW) method computes the correlation at time point  $i$  as

$$\rho_{\mathbf{x}, \mathbf{y}}(i) = \frac{\sum_{j \in W_m(i)} (x_j - \bar{x}_i)(y_j - \bar{y}_i)}{\sigma_{\mathbf{x}}(i)\sigma_{\mathbf{y}}(i)},$$

where  $\bar{x}_i$  and  $\bar{y}_i$  are the weighted means of  $\mathbf{x}$  and  $\mathbf{y}$  within window  $W_m(i)$

$$\bar{x}_i = \frac{1}{m} \sum_{j \in W_m(i)} x_j$$

and  $\sigma_{\mathbf{x}}^2(i)$  and  $\sigma_{\mathbf{y}}^2(i)$  are the weighted variances given by

$$\sigma_{\mathbf{x}}^2(i) = \frac{1}{m} \sum_{j \in W_m(i)} (x_j - \bar{x}_i)^2.$$

Figure 1 displays an example of the SW-method with window sizes 15 and 20 TRs. The SW-method suffers from severe zig-zag patterns caused by the use of the discrete window, which could not be effectively reduced even if we increase the window size from 15 to 20 TRs.

*Tapered sliding window method.* In [7], the authors suggested to convolve the square window with a Gaussian kernel, called tapered square window, so that the data points will gradually enter and exit from the tapered window when moving across

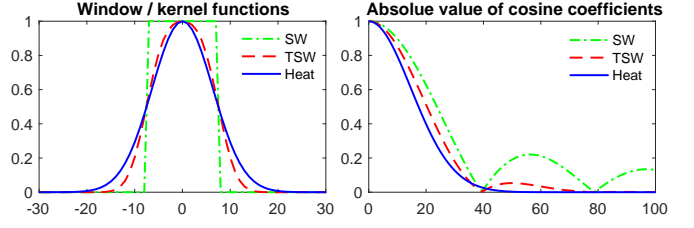


Fig. 2. square window, tapered window and heat kernel with the same size or FWHM. The heat kernel is defined on a circle continuously without endpoint or boundary. Here, we only showed the kernel at central 60 time points. Right: absolute values of the first 100 cosine coefficients of the widow and kernel functions. The sidelobes of the window functions in spectral domain will cause high-frequency noise or fluctuations remaining.

time [12]. The correlation computed using the tapered sliding window (TSW) is given by

$$\rho_{\mathbf{x}, \mathbf{y}}(i) = \frac{\sum_{j \in W_m(i)} \omega_j(x_j - \bar{x}_i)(y_j - \bar{y}_i)}{\sigma_{\mathbf{x}}(i)\sigma_{\mathbf{y}}(i)}.$$

$\bar{x}_i$  and  $\bar{y}_i$  are the means of  $\mathbf{x}$  and  $\mathbf{y}$  in  $W_m(i)$  weighted by some weight  $\omega_j$  satisfying  $\sum_j \omega_j = 1$ , i.e.,

$$\bar{x}_i = \sum_{j \in W_m(i)} \omega_j x_j,$$

and  $\sigma_{\mathbf{x}}^2(i)$  and  $\sigma_{\mathbf{y}}^2(i)$  are the variances weighted by

$$\sigma_{\mathbf{x}}^2(i) = \sum_{j \in W_m(i)} \omega_j (x_j - \bar{x}_i)^2.$$

Figure 1 shows the TSW-method using the square window of sizes 15 and 20 TRs convolved with the Gaussian kernel with bandwidth 3 TRs [12]. The TSW-method was able to reduce the zig-zag pattern in SW-method significantly but still showing rapid high frequency fluctuations. There were even more high-frequency fluctuations in some time intervals when larger window is used indicating that they are in fact artifacts produced by the use of discrete windows. Such zig-zag pattern and high-frequency fluctuations in the SW- and TSW-methods are caused by the sidelobes of the window functions in spectral domain [16] (Figure 2). To address the problem caused by using a window function with finite support, we propose to use a kernel function without boundary that is defined on the whole domain of the data.

### III. METHODS

In this section, we firstly define the heat kernel on a circle, which will be used in the proposed windowless dynamic correlation. Next, the integral version of the Pearson correlation is introduced and extended to the windowless dynamic correlation by the use of a kernel function without end endpoint or boundary. As the kernel is constructed by the cosine basis, the windowless dynamic correlation can be expressed in terms of the cosine basis functions.

#### A. Heat kernel convolution on a circle

*Diffusion on  $[0, 1]$ .* Consider 1D heat diffusion of time series data  $f(t)$  on unit interval  $[0, 1]$ :

$$\frac{\partial}{\partial s} h(t, s) = \frac{\partial^2}{\partial t^2} h(t, s) \quad (1)$$

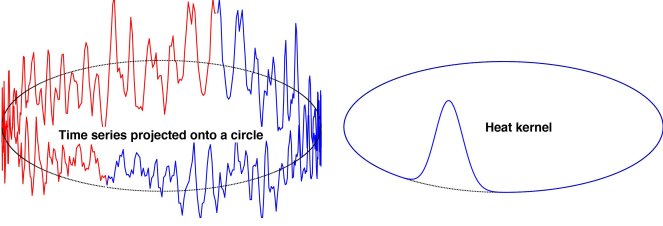


Fig. 3. Left: time series data (blue) projected onto a circle by connecting its mirror reflection (red). Right: heat kernels defined on the circle. Only plotted  $K_s(t, t')$  at  $t = 0$ .

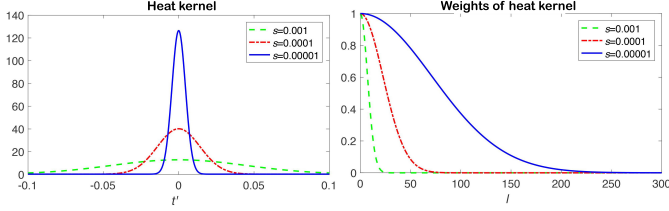


Fig. 4. Left: heat kernels  $K_s(t, t')$  at  $t = 0$  with different diffusion time or bandwidth  $s$ . The heat kernel has larger FWHM when  $s$  increases. Right: weights  $e^{-l^2\pi^2 s}$  of the heat kernels. As  $s$  increases, the weights in the high frequencies become smaller compared to low frequencies, and more high-frequency components will be smoothed out.

at diffusion time  $s$  with initial condition  $h(t, s = 0) = f(t)$ . The unique solution is given by the weighted cosine series representation (WCSR) [17], [28]

$$h(t, s) = \sum_{l=0}^{\infty} e^{-l^2\pi^2 s} c_{fl} \psi_l(t),$$

where  $\psi_0(t) = 1$ ,  $\psi_l(t) = \sqrt{2} \cos(l\pi t)$  are the cosine basis and  $c_{fl}$  are the cosine series coefficients of  $f$ :

$$c_{fl} = \int_0^1 f(t) \psi_l(t) dt.$$

*Diffusion on a circle.* To avoid the boundary effect as in the SW- and TSW-methods [27], we project  $f(t)$  defined in  $[0, 1]$  onto the circle  $\mathcal{C}$  by connecting its mirror reflection in the following way (Figure 3):

$$g(t) = f(t) \text{ if } t \in [0, 1], \quad g(t) = f(2 - t) \text{ if } t \in [1, 2].$$

Then  $g$  is a periodic function defined on the circle  $\mathcal{C}$  with circumference 2. Then we solve diffusion equation (1) with initial condition  $h(t, s = 0) = g(t)$  on circle  $\mathcal{C}$ . It can be shown that solution is given by heat kernel convolution

$$h(t, s) = \int_0^1 K_s(t, t') f(t') dt', \quad (2)$$

where heat kernel  $K_s(t, t')$  is defined as

$$K_s(t, t') = \sum_{l=0}^{\infty} e^{-l^2\pi^2 s} \psi_l(t) \psi_l(t'). \quad (3)$$

The diffusion time  $s$ , also referred to as the bandwidth of the heat kernel, controls the amount of diffusion. Unlike window functions, there is no endpoint or boundary in the heat kernel

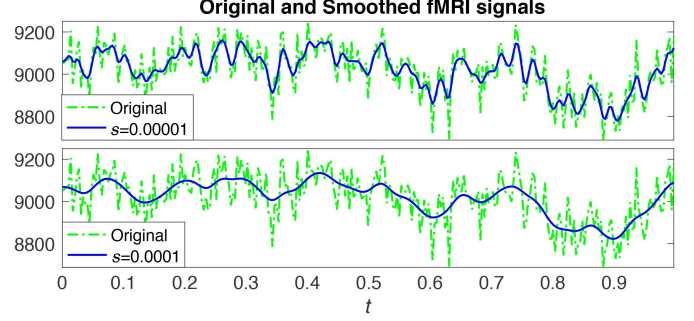


Fig. 5. Original and smoothed fMRI time series computed by the heat kernel convolution with degree  $L = 295$  and heat kernel bandwidth  $s = 10^{-5}$  and  $10^{-4}$ . As  $s$  increases, the amount of smoothing increases.

defined on a circle (Figure 3) with non-zero values over the entire circle. The heat kernel does not have the sidelobe problem (Figure 2) as in the discrete window functions. Figure 4 shows the heat kernels  $K_s(t, t')$  versus  $t'$  at fixed  $t = 0$  and the weights  $e^{-l^2\pi^2 s}$  for different bandwidth  $s$ .

In the numerical implementation, the heat kernel smoothing of  $g(t)$  is estimated by the WCSR of  $f(t)$  with degree  $L$ :

$$h(t, s) = \sum_{l=0}^L e^{-l^2\pi^2 s} c_{fl} \psi_l(t),$$

where  $c_{fl}$  are the cosine series coefficients of  $f(t)$  estimated via the least squares method [17]. In this study, we use degree  $L = T$ . Figure 5 shows the original and smoothed fMRI time series of  $T = 295$  points, where heat kernel smoothing is realized by the WCSR with  $L = 295$  and  $s = 10^{-5}$  and  $10^{-4}$ . When  $s$  increases, the amount of smoothing increases.

### B. Integral version of Pearson correlation

In this section, we introduce the integral generalization of the Pearson correlation and analyze its convergence to the traditional Pearson correlation. The method is then applied in computing windowless correlations. Given two discrete data  $\mathbf{x} = (x_0, x_1, \dots, x_{T-1})$  and  $\mathbf{y} = (y_0, y_1, \dots, y_{T-1})$ , the Pearson correlation of  $\mathbf{x}$  and  $\mathbf{y}$  is defined as

$$\rho_{\mathbf{x}, \mathbf{y}} = \frac{\sum_{i=0}^{T-1} (x_i - \bar{x})(y_i - \bar{y})}{\sqrt{\sum_{i=0}^{T-1} (x_i - \bar{x})^2} \sqrt{\sum_{i=0}^{T-1} (y_i - \bar{y})^2}},$$

where  $\bar{x} = \sum_{i=0}^{T-1} x_i / T$  and  $\bar{y} = \sum_{i=0}^{T-1} y_i / T$ .

Consider continuous signals  $x(t)$  and  $y(t)$  in  $L_2[0, 1]$ . Then the integral version of Pearson correlation between  $x(t)$  and  $y(t)$  is defined as

$$r_{x(t), y(t)} = \frac{\int_0^1 (x(t) - \mu_x)(y(t) - \mu_y) dt}{\sqrt{\int_0^1 (x(t) - \mu_x)^2 dt} \sqrt{\int_0^1 (y(t) - \mu_y)^2 dt}},$$

where  $\mu_x = \int_0^1 x(t) dt$  and  $\mu_y = \int_0^1 y(t) dt$  are the means of  $x(t)$  and  $y(t)$ . As the sample size  $T$  increases, we have  $\rho_{\mathbf{x}, \mathbf{y}} \rightarrow r_{x(t), y(t)}$ . Through the paper, we will use the integral version of Pearson correlation. The convergence is demonstrated in the following example.

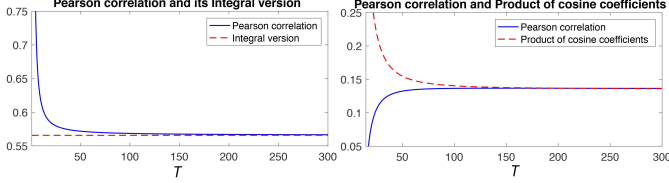


Fig. 6. Left: Comparison of the Pearson correlation and its integral version. The Pearson correlation approaches the integral version as number of samples  $T$  increases. Right: Comparison of the Pearson correlation and the product of cosine series coefficients. The error decreases when  $T$  increases because the discrete cosine series approaches the continuous cosine series.

**Example 1.** Consider two continuous signals

$$\begin{aligned}x(t) &= 1 - \cos(\pi t) - \cos(2\pi t), \\y(t) &= -0.8\sqrt{2}\cos(2\pi t) + 0.6\sqrt{2}\cos(3\pi t).\end{aligned}$$

The integral version of Pearson correlation between  $x(t)$  and  $y(t)$  is exactly given by  $r_{x(t),y(t)} = \frac{1}{\sqrt{2}}0.8 = 0.5657$  (dashed red line in Figure 6-left). If we let  $x_i = x(t_i)$  and  $y_i = y(t_i)$  with  $t_i = i/T$ , the Pearson correlation  $\rho_{x,y}$  (solid blue line) converges to  $r_{x(t),y(t)}$  as  $T$  increases. When  $T = 295$ , the error is less than  $9.1 \times 10^{-4}$ .

**Correlation as the product of cosine coefficients.** If we use the cosine series representation (CSR) on time series  $x(t)$  and  $y(t)$ , we can represent the integral correlation as the product of CSR coefficients [17]. Consider the CSR of  $x(t)$  and  $y(t)$  given by

$$x(t) = \sum_{l=0}^{\infty} c_{xl} \psi_l(t), \quad y(t) = \sum_{l=0}^{\infty} c_{yl} \psi_l(t),$$

where  $c_{xl} = \int_0^1 x(t) \psi_l(t) dt$  and  $c_{yl} = \int_0^1 y(t) \psi_l(t) dt$  are the cosine series coefficients. Since  $\psi_0(t) = 1$ , the means of  $x(t)$  and  $y(t)$  are the first cosine series coefficients, i.e.,  $\mu_x = c_{x0}$  and  $\mu_y = c_{y0}$ . Due to the orthonormality of  $\psi_l(t)$ , the integral version of Pearson correlation can be computed by the cosine series coefficients as

$$r_{x(t),y(t)} = \frac{\sum_{l=1}^{\infty} c_{xl} c_{yl}}{\sqrt{\sum_{l=1}^{\infty} c_{xl}^2} \sqrt{\sum_{l=1}^{\infty} c_{yl}^2}}.$$

If  $x(t)$  and  $y(t)$  are normalized such that  $\sum_{l=1}^{\infty} c_{xl}^2 = 1$  and  $\sum_{l=1}^{\infty} c_{yl}^2 = 1$ , and then the integral version of Pearson correlation can be further given by the product

$$r_{x(t),y(t)} = \sum_{l=1}^{\infty} c_{xl} c_{yl}.$$

**Example 2.** Given discrete data  $\mathbf{x}$  and  $\mathbf{y}$  computed from

$$x_i = t_i \sin(6\pi t_i^2), \quad y = t_i^2 \cos(5\pi t_i),$$

the solid line in Figure 6-right shows the Pearson correlation while the dashed line shows the product of cosine series coefficients. The error decreases when  $T$  increases and is  $3 \times 10^{-4}$  when  $T = 295$ .

### C. Windowless dynamic correlation

Consider time series data  $x(t)$  and  $y(t)$  in interval  $[0, 1]$ . To avoid the discontinuity of data at the boundaries  $t = 0, 1$ , the data will be mirror reflected to form periodic data on circle  $\mathcal{C}$  with circumference 2 such that

$$\tilde{x}(t) = x(t) \text{ if } t \in [0, 1], \quad \tilde{x}(t) = x(2-t) \text{ if } t \in [1, 2].$$

$\tilde{y}(t)$  is defined using  $y(t)$  similarly.

Instead of using square windows, we propose to use kernel  $w(t, t')$  defined on circle  $\mathcal{C}$  as follows. We start with defining kernel on interval  $[0, 1]$  and then extend the definition to  $\mathcal{C}$ :

$$\int_0^1 w(t, t') dt' = 1 \text{ for any } t.$$

We further assume the kernel can be decomposed as

$$w(t, t') = \sum_{l=0}^{\infty} c_{wl} \psi_l(t) \psi_l(t'),$$

where  $\psi_l$  are the cosine basis  $\psi_0(t) = 1$ ,  $\psi_l(t) = \sqrt{2} \cos(l\pi t)$ . Heat kernel is such a kernel defined as

$$w(t, t') = K_s(t, t') = \sum_{l=0}^{\infty} e^{-l^2 \pi^2 s} \psi_l(t) \psi_l(t'),$$

with  $c_{wl} = e^{-l^2 \pi^2 s}$ . Due to the symmetry of cosine basis functions,  $\psi_l(t') = \psi_l(2-t')$ , we have  $w(t, t') = w(t, 2-t')$  for any  $t$ . Then we have

$$\int_0^2 w(t, t') dt' = \int_0^1 w(t, t') dt' + \int_0^1 w(t, 2-t') dt' = 2.$$

Similarly, we also have

$$\begin{aligned}&\int_0^2 w(t, t') \tilde{x}(t') dt' \\&= \int_0^1 w(t, t') \tilde{x}(t') dt' + \int_0^1 w(t, 2-t') \tilde{x}(2-t') dt' \\&= 2 \int_0^1 w(t, t') \tilde{x}(t') dt' = 2 \int_0^1 w(t, t') x(t') dt'\end{aligned}$$

and

$$\int_0^2 w(t, t') \tilde{y}(t') dt' = 2 \int_0^1 w(t, t') y(t') dt'.$$

Since correlation is invariant under scaling, the windowless dynamic correlation between  $\tilde{x}(t)$  and  $\tilde{y}(t)$  over the circle  $\mathcal{C}$  is equivalent to the windowless dynamic correlation between  $x(t)$  and  $y(t)$  over  $[0, 1]$ :

$$r_{x,y}(t) = \frac{\int_0^1 w(t, t') x(t') y(t') dt' - \mu_x(t) \mu_y(t)}{\sigma_x(t) \sigma_y(t)}, \quad (4)$$

where

$$\begin{aligned}\mu_x(t) &= \int_0^1 w(t, t') x(t') dt', \\ \sigma_x^2(t) &= \int_0^1 w(t, t') x^2(t') dt' - \mu_x^2(t)\end{aligned}$$

are the dynamic mean and variance of  $x(t)$ .  $\mu_y(t)$  and  $\sigma_y^2(t)$  are defined similarly.

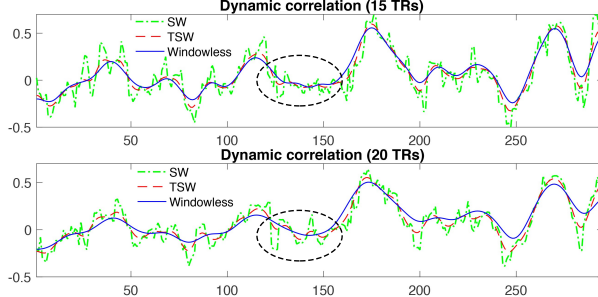


Fig. 7. The SW-, TSW- and proposed windowless methods using either window and kernel function of the same size with FWHM 15 (top) and 20 (bottom) TRs. The windowless method eliminated most of the zig-zag pattern and high-frequency fluctuations in the SW- and TSW-methods.

Since kernel  $w$  is expressed in terms of the cosine basis functions, the convolution of  $w$  and  $f$  can be rewritten as

$$\int_0^1 w(t, t') f(t') dt' = \sum_{l=0}^{\infty} c_{wl} c_{fl} \psi_l(t),$$

where  $c_{fl} = \int_0^1 f(t') \psi_l(t') dt'$  is the cosine series coefficients. Suppose  $c_{xl}$ ,  $c_{yl}$ ,  $c_{xyl}$ ,  $c_{xxl}$  and  $c_{yyl}$  denote the cosine series coefficients of  $x(t)$ ,  $y(t)$ ,  $x(t)y(t)$ ,  $x^2(t)$  and  $y^2(t)$  in representing them as, for instance,

$$x(t) = \sum_{l=0}^{\infty} c_{xl} \psi_l(t), \quad x(t)y(t) = \sum_{l=0}^{\infty} c_{xyl} \psi_l(t).$$

Then, the windowless dynamic correlation correlation (4) can be written as

$$r_{x,y}(t) = \frac{\sum_{l=0}^{\infty} c_{wl} c_{xyl} \psi_l(t) - \mu_x(t) \mu_y(t)}{\sigma_x(t) \sigma_y(t)}, \quad (5)$$

with

$$\begin{aligned} \mu_x(t) &= \sum_{l=0}^{\infty} c_{wl} c_{xl} \psi_l(t), \\ \sigma_x^2(t) &= \sum_{l=0}^{\infty} c_{wl} c_{xxl} \psi_l(t) - \mu_x^2(t). \end{aligned}$$

Figure 7 shows the windowless dynamic correlation using the heat kernel with  $s = 2.3 \times 10^{-4}$  and  $s = 4.1 \times 10^{-4}$ , which give FWHM 15 and 20 TRs respectively. The proposed windowless method eliminated most of the zig-zag pattern and high-frequency fluctuations in the SW- and TSW-methods, and the bandwidth  $s$  of the heat kernel controls the smoothness of the estimated dynamic correlation.

#### D. Clustering of the state space

The estimated dynamic correlations will be used in determining the state spaces. Assume there are  $n$  subjects in the dataset. By computing the dynamic correlations between  $p$  brain regions, we have  $p \times p$  dynamic correlation matrices  $C_i(t_j)$  for the  $i$ -th subject at time points  $t = t_1, \dots, t_T$ . Let  $\mathbf{d}_{ij}$  denote the vectorization of  $p \times p$  matrix  $C_i(t_j)$  such that  $\mathbf{d}_{ij}$  is a vector of size  $p^2$ . The collection of  $\mathbf{d}_{ij}$  over time and subjects is feed into the  $k$ -means clustering following [26] in identifying the recurring brain connectivity states that are

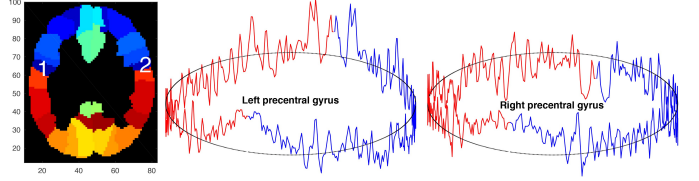


Fig. 8. Left: brain regions using AAL template. The left and right precentral gyri regions are marked as regions 1 and 2. Right: average fMRI signals within left and right precentral gyri (blue) projected onto a circle and connected with their mirror reflections (red).

common across subjects. The optimal number of cluster  $k$  is determined by the elbow method.

## IV. APPLICATION

### A. Dataset and preprocessing

Resting-state (rs) functional magnetic resonance images (rs-fMRI) were collected on a 3T MRI scanner (Discovery MR750, General Electric Medical Systems, Milwaukee, WI, USA) with a 32-channel RF head coil array. T1-weighted structural images ( $1 \text{ mm}^3$  voxels) were also acquired axially with an isotropic 3D Bravo sequence ( $TE = 3.2 \text{ ms}$ ,  $TR = 8.2 \text{ ms}$ ,  $TI = 450 \text{ ms}$ , flip angle =  $12^\circ$ ). T2\*-weighted gradient-echo echo-planar pulse sequence images were collected during resting state and the task with  $TE = 20 \text{ ms}$ ,  $TR = 2000 \text{ ms}$ , and flip angle =  $60^\circ$ . The functional scans were undergone a series of data reduction, correction, registration, and spatial and temporal preprocessing [29]. The resulting rs-fMRI consists of  $91 \times 109 \times 91$  isotropic voxels at 295 time points. Excluding one subject that has no fMRI signals in two brain regions, the average fMRI signals of 479 healthy subjects ranging in age from 13 to 25 years were used in our study.

We employed the Automated Anatomical Labeling (AAL) brain template to parcellate the brain volume into 116 non-overlapping anatomical regions [30]. The fMRI data were averaged across voxels within each brain region, resulting in 116 average fMRI signals with 295 time points for each subject.

### B. Dynamic functional connectivity

For each subject, the 116 average rs-fMRI signals were scaled to fit to unit interval  $[0, 1]$ . To reduce the boundary effect, we continuously connected fMRI with its mirror reflection at the end points  $t = 0$  and  $t = 1$ . Figure 8 displays the average fMRI in the left and right precentral gyri connected at the first ( $t = 0$ ) and the 295-th scan ( $t = 1$ ). This has the effect of making fMRI circular data on a circle with circumference 2.

We evaluated the dynamic functional connectivity between brain regions through the dynamic correlations computed by the SW-, TSW-, and the proposed windowless methods. Smaller window size can capture more short-lived variations in brain connectivity than larger windows [9], but will increase the risk of creating high-amplitude variations and spurious fluctuations even when the connectivity is actually static [11], [12], [31]. In [32], it was shown that the accuracy

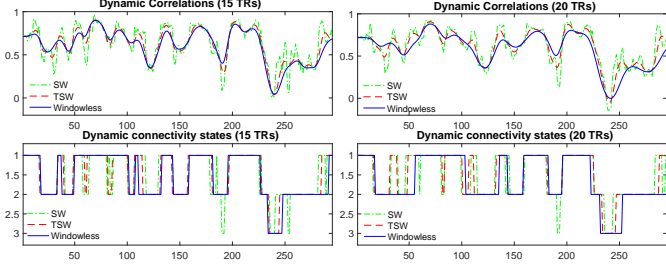


Fig. 9. Dynamic interhemispheric correlations (top) between the average fMRI signals of left and right precentral gyri and the corresponding dynamic connectivity states (bottom). The SW-, TSW- and proposed windowless methods with FWHM 15 (left) and 20 (right) TRs were used. The windowless method estimated the dynamic correlations more smoothly over time and has the least number of rapid state changes.

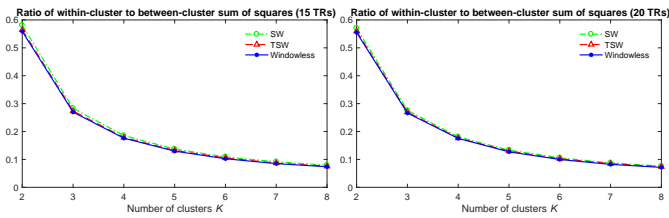


Fig. 10. The ratio of within-cluster to between-cluster sum of squared distances versus the number of clusters  $K = 2, \dots, 8$  for window/kernel FWHM 15 (left) and 20 (right) TRs. By the elbow method, three clusters were chosen since the slope changes the most drastically from steep to shallow at the elbow point  $K = 3$ .

of brain-state classification remained high with imaging as short as 30–60 seconds. Such window sizes can capture variability not found in larger windows [33], [34] and have been widely utilized in the previous studies [3], [11], [15], [18], [31], [35]–[37]. In this study, square windows of size 15 and 20 TRs (i.e., 30 and 40 seconds) were used in the SW-method. Following [7], [12], the tapered windows in the TSW-method were obtained by convolving the square windows with a Gaussian kernel with bandwidth 3 TRs. In the proposed windowless method, we used heat kernels with bandwidth  $s = 2.3 \times 10^{-4}$  and  $4.1 \times 10^{-4}$ . Then, the window and kernel functions in all the three methods have the same FWHM (i.e., 15 and 20 TRs).

**Dynamic interhemispheric connectivity.** Excluding the 8 vermis regions that do not belong to the left or right brain hemisphere, we computed the 54 dynamic interhemispheric correlations of the 54 hemispherically paired brain regions. Figure 9 displays the result of the left and right precentral gyri of one subject. The SW-method showed severe zig-zag pattern. The proposed windowless method has much fewer high-frequency fluctuations and estimated the dynamic correlations more smoothly over time.

**Dynamic whole-brain connectivity.** For each subject, we measure the dynamic whole-brain connectivity by the  $116 \times 116$  dynamic correlation matrix computed from the 116 average fMRI signals. The dynamic correlation matrix of one subject is shown in Figure 11, where the proposed windowless method

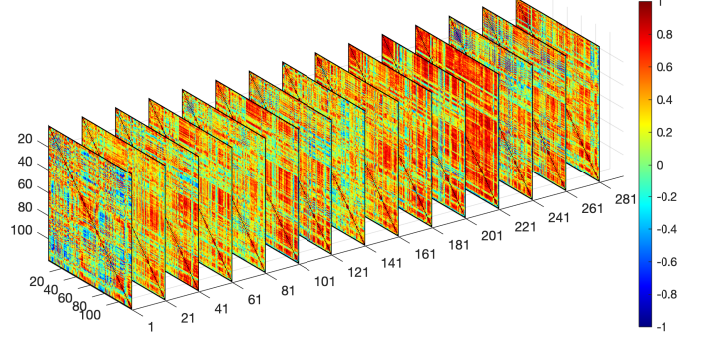


Fig. 11.  $116 \times 116$  dynamic correlation matrices of one subject at time points 1, 21, 41, ..., 281 using the proposed windowless method with FWHM 15 TRs.

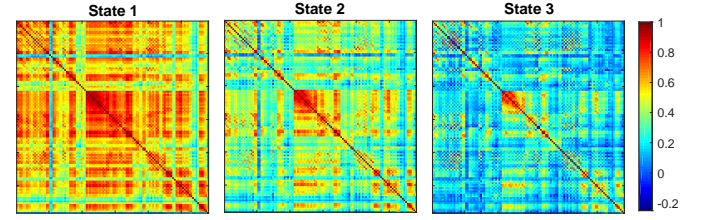


Fig. 12. The average correlation matrices (cluster centroids) of the three states. The values of average correlations range from 0.03 to 0.98 in state 1, from -0.12 to 0.95 in state 2, and from -0.22 to 0.89 in state 3. Only the windowless method with FWHM 20 TR was plotted because different methods have similar result. Within each state, the absolute errors between the centroids obtained from different methods are all smaller than 0.075.

with FWHM 15 TRs was used. Since the dynamic correlations varies smoothly, we only showed the result every 20 time points.

### C. Estimation of distinct state space

The baseline  $k$ -means clustering was used to identify the distinct states that repetitively occur throughout the time course and are common across subjects. These discrete states serve as the basis of investigating brain connectivity. We applied the  $k$ -means clustering to the dynamic correlations to compare the performance of the proposed windowless method against the SW- and TSW-methods. The clustering was repeated 100 times with different initial centroids, and the best result with the lowest sum of squared distances was chosen. To determine the number of clusters  $K$ , we applied the elbow method which was widely used in literature such as [7], [13], [15], [26], [37], [38]. For each value of  $K$ , we computed the within-cluster and between-cluster sums of squares, i.e., sums of squared Euclidean distances between centroids and the data points within and outside the clusters. Then, we plotted the ratio of within-cluster to between-cluster sum of squares for  $K = 2, \dots, 8$  (Figure 10). By the elbow method, we chose  $K = 3$  which gives the largest slope change from steep to shallow in the elbow plot. Three clusters (partition states) were also adopted by many previous studies [26], [39], [40].

**Dynamic interhemispheric connectivity states.** For each of the 54 interhemispheric pairs, the dynamic correlations at

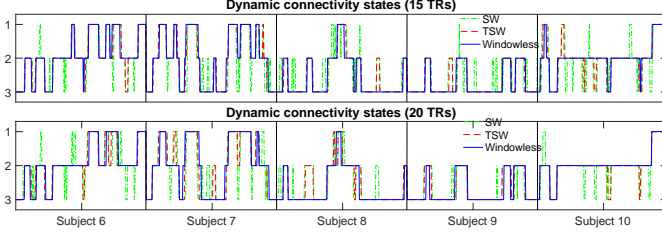


Fig. 13. Dynamic whole-brain connectivity states of the 6th-10th subjects when the SW-, TSW and proposed windowless methods with FWHM 15 (top) and 20 TRs (bottom). The windowless method eliminated many rapid state changes in the SW- and TSW-methods.

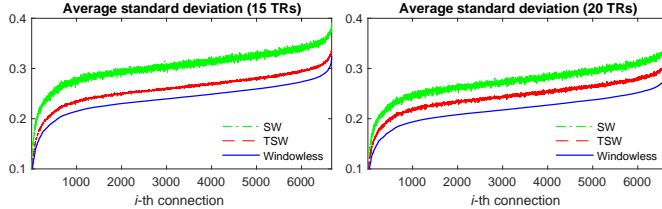


Fig. 14. The average standard deviations of the dynamic correlations of the 6670 brain connections, displayed in order of the result of the windowless method. For FWHM 15 TRs (left), from the SW-method, the average standard deviation is reduced between 10.6% and 23.6% by the TSW-method, and reduced between 15.2% and 33.5% by the windowless method. For 20 TRs (right), the average standard deviation is reduced between 8% and 16.6% by the TSW-method, and reduced between 14.4% and 31.6% by the windowless method.

295 time points were concatenated across 479 subjects, which resulted in  $295 \cdot 479 = 141305$  total number of correlations that served as the input to  $k$ -means clustering. The dynamic interhemispheric connectivity states of the left and right precentral gyri of one subject are displayed in Figure 9. The windowless method eliminated many state changes, i.e., transitions, in the SW- and TSW-methods caused by the zig-zag pattern and high-frequency fluctuations in dynamic correlations.

**Dynamic whole-brain connectivity states.** We also applied the  $k$ -means clustering to identify the dynamic connectivity states of the whole-brain network. This was done by concatenating  $116 \times 116 \times 295$  dynamic correlation matrices across all 479 subjects, which results in  $259 \cdot 479 = 141305$  correlation matrices, each of which is of size  $116 \times 116$ . We vectorized each correlation matrix to a  $116^2$ -dimensional vector, and all the 141305 vectors are served as the input data points of the  $k$ -means clustering algorithm. The averages of the dynamic correlation matrices within each state (i.e., cluster centroids) of the windowless method are displayed in Figure 12. The dynamic connectivity states of five representative subjects are shown in Figure 13. The windowless method has the least number of rapid changes in the state space.

#### D. Results

We compared the proposed windowless method to the SW- and TSW-methods in the variability of the dynamic

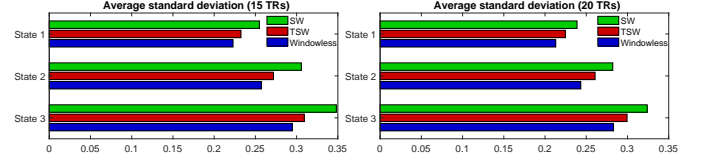


Fig. 15. The average standard deviation within each state. For FWHM 15 TRs (left), from the SW-method, the average standard deviations are reduced 8.8%, 11% and 11.2% by the TSW-method, and reduced 12.5%, 15.8% and 15.3% by the proposed windowless method. For 20 TRs (right), the average standard deviations are reduced 7.5%, 7.6%, and 5.9% by the TSW-method, and reduced 12.6%, 13.8%, and 10.8% by the windowless method.

correlation matrices and the transition probability of dynamic connectivity states. Then, we used the proposed windowless method to show the interhemispheric symmetry of paired brain regions from the dynamic interhemispheric correlations, and the strongest connections in brain networks from the dynamic correlation matrices.

**Variability of each connection.** There are 116 nodes (brain regions) in the brain networks and  $116 \cdot 115/2 = 6670$  brain connections, i.e. the 6670 entries of the upper (or lower) triangular part of correlation matrix. For each subject and each connection, we computed the standard deviations of dynamic correlations across 295 time points. Then, we averaged the standard deviations across all 479 subjects (Figure 14). The windowless method has the smallest variability in each connection.

**Variability within each state.** The dynamic correlation matrices of each subject were partitioned into three states. Within each state, we computed the standard deviation of correlations for each brain connection over all time points and subjects and then averaged them across all brain connections (Figure 15). The proposed windowless method shows lower variability within each state than the SW- and TSW-methods.

**Transition probability.** We computed the state transitions to reveal the interactions between different brain states [41]. They can be modeled as a Markov chain [42]. For subject  $i$ , the transition probability of moving from state  $k_1$  to state  $k_2$  is computed by

$$P(s_{ij} = k_2 | s_{i,j-1} = k_1), \quad (6)$$

where  $s_{ij} \in \{1, 2, 3\}$  are the state labels obtained from  $k$ -means clustering. Figure 16 shows the average transition probability over all subjects. Each subject remained in the same state for a long period of time before transitioning to other brain state. The very low average transition probabilities between state 1 and state 3 show the inability of transitioning directly between these two states. The proposed windowless method has the lowest transition probabilities between different states and the highest probabilities of remaining in the same state.

**Interhemispheric symmetry.** Figure 17 shows the average correlation and the occupancy rate [43], [44] of each state and

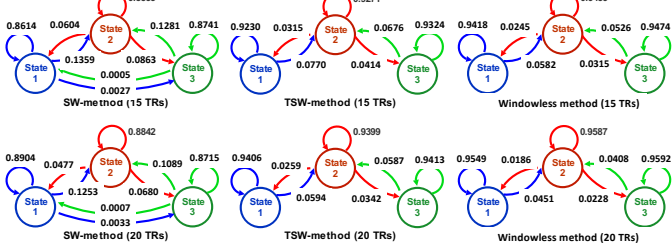


Fig. 16. Transition probabilities averaged across all 479 subjects. The transition probabilities between different states decrease when larger window or bandwidth (bottom) is used, and are the lowest when the proposed windowless method (right) is used. The probabilities of remaining in the same state increase when larger window or bandwidth (bottom) is used, and are the highest when the windowless method (right) is used.

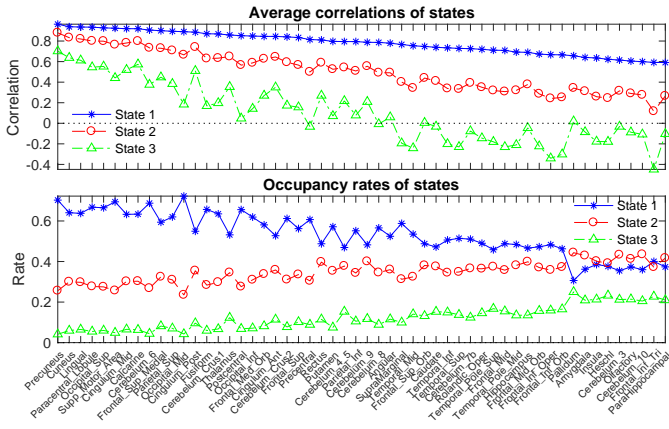


Fig. 17. Dynamic interhemispheric correlations: the average correlations (top) of the three states in order of the values of the average correlations of state 1, and the occupancy rates (bottom) of the three states. The proposed windowless method with FWHM 20 TRs was used. Each interhemispheric connectivity has different occupancy rate because  $k$ -means clustering was applied separately.

interhemispheric connectivity, where the proposed windowless method with FWHM 20 TRs was used. The occupancy rate of state  $k$  is computed as

$$\frac{1}{nT} \sum_{i=1}^n \sum_{j=1}^T (s_{ij} = k),$$

where  $n = 479$  subjects and  $T = 295$  time points. The state space of each interhemispheric connectivity was estimated separately, and thus has different occupancy rates. Precuneus, cuneus, lingual gyrus, paracentral lobule and superior occipital are the five brain regions having the highest interhemispheric correlations in the state space, and thus have the strongest symmetry compared to other brain regions. The parahippocampal gyrus, inferior frontal gyrus (pars triangularis), lobule X of cerebellar hemisphere, olfactory cortex and lobule III of cerebellar hemisphere are the five brain regions having the weakest interhemispheric symmetry.

**Strong connections in whole-brain networks.** From the average correlation matrices of the three states (Figure 12), we listed the first 50 brain connections (matrix entries) having the highest average correlations in state 1 (Figure 18). 11 of the 50 connections are hemispherically paired regions.

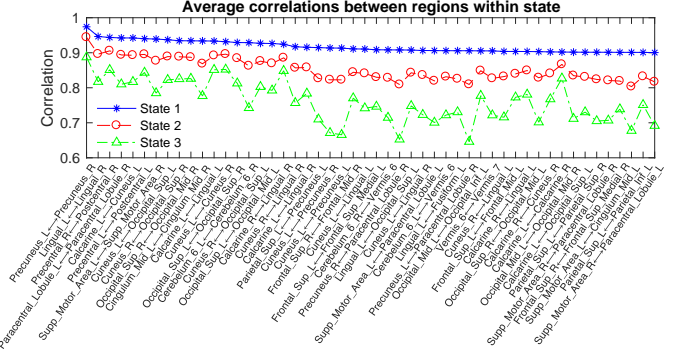


Fig. 18. Dynamic correlation matrices: the average correlations of the three states in order of the values of the average correlations of state 1. The proposed windowless method with FWHM 20 TRs was used. Only showed the results of the first 50 connections with highest average correlations in state 1. All the connections shared the same occupancy rate: 0.23, 0.43 and 0.34 for states 1, 2 and 3 respectively.

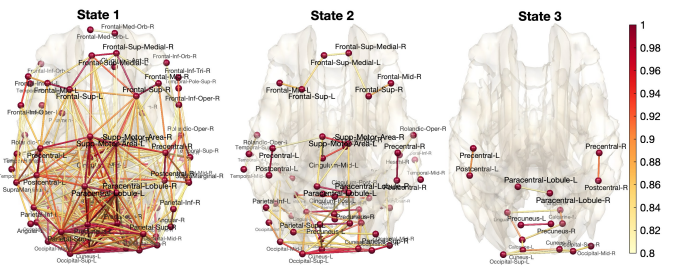


Fig. 19. The average correlation matrices (cluster centroids) of the three states using the windowless method with FWHM 20 TRs. Only strong connections with correlation larger than 0.8 are displayed. State 1 includes all the strong connections in states 2 and 3, and state 2 includes all the strong connections in state 1. Left and right precunei, right superior parietal lobule, left cuneus and right lingual gyrus are the five most connected regions in state 1.

Among these 11 paired regions, calcarine sulci, cunei, lingual gyri, superior occipital gyri and middle occipital gyri also have strong connections between each other. Figure 19 is an alternative visualization of the average correlation matrices, showing strong connections with correlation values larger than 0.8.

## V. DISCUSSIONS

**Brain state transition probability.** The resting-state networks tend to remain in the same state for a long period before the transition to another state [7], [9], [13], [45], [46]. In this study, the proposed windowless method showed a longer stability (less rapid changes) in the state space and exhibited a higher probability of remaining in the same state compared to the SW- and TSW-methods.

**Dynamic whole-brain connectivity.** In this study, the average correlation matrices (cluster centroids) of the three states follow similar connectivity patterns to the previous study [47] in which the AAL parcellation and  $k$ -means clustering were also used except that four states were adopted. Besides, the three states shared similar connectivity pattern except for different overall correlation values. This may be due to the small number of clusters, which can also be observed in

[48]. We showed that different methods (SW-, TSW-, and windowless) and different window size or kernel bandwidth (15 and 20 TRs) have little influence to the average correlation matrices within states. However, the proposed windowless method achieved smaller noise-induced variability of correlations within states.

The average correlation matrices of the three states showed relative higher correlations between calcarine sulci, cunei, lingual gyri, superior occipital gyri and middle occipital gyri. All these regions belong to the occipital lobe and are the nodes of the visual network, which is one of the resting state networks [49], [50]. Compared to other resting state networks, the visual network has the strongest connectivity across different states, followed by the somatomotor network.

*Dynamic interhemispheric connectivity.* Previous studies have demonstrated high correlations between hemispherical paired brain regions [51]–[54]. In [51], it was shown that the median cingulate and paracingulate gyri, thalamus, precuneus, anterior cingulate and paracingulate gyri are some of the regions with highest interhemispheric correlations. [52] demonstrated higher interhemispheric correlation in primary sensory-motor cortices, including postcentral gyrus, occipital pole, lingual gyrus, cuneal cortex, precentral gyrus among other regions. In [54], the authors showed the trend toward higher interhemispheric connectivity near the midline, such as the frontal pole, occipital cortex and medial parietal lobe, deep gray nuclei, and cerebellum. Further, it was showed that younger subjects have higher interhemispheric correlations in the supplementary motor area, precuneus and occipital lobe.

While most of previous research focuses on the static functional connectivity, in this paper, the dynamic change of interhemispheric connectivity was analyzed and further summarized into three distinct states. The results showed that hemispherically paired regions with high correlations in state 1 also have high correlations in state 2, where states 1 and 2 dominate the brain state with occupancy rate over 75%. Consistent with previous studies, we observed relatively higher interhemispheric correlations in precuneus, cuneus, lingual gyrus, paracentral lobule, superior occipital, supplementary motor area, midcingulate area, calcarine sulcus among other regions. Many of these regions are close to the midline.

#### DECLARATION AND ACKNOWLEDGEMENTS

The authors have no conflict of interest to declare. The data that support the findings of this study are available on request from the corresponding author.

We would like to thank Siti Balqis Samdin, Chee-Ming Ting and Hernando Ombao of KAUST and Martin Lindquist of Johns Hopkins University for providing valuable discussion and support on state space modeling.

#### REFERENCES

- [1] C. Chang and C. Glover, “Time-frequency dynamics of resting-state brain connectivity measured with fMRI,” *NeuroImage*, vol. 50, no. 1, pp. 81–98, 2010.
- [2] R. Hutchison *et al.*, “Dynamic functional connectivity: Promise, issues, and interpretations,” *NeuroImage*, vol. 80, pp. 360–378, 2013.
- [3] R. Hutchison and J. Morton, “Tracking the brain’s functional coupling dynamics over development,” *Journal of Neuroscience*, vol. 35, no. 17, pp. 6849–6859, 2015.
- [4] M. Preti, T. Bolton, and D. Van De Ville, “The dynamic functional connectome: State-of-the-art and perspectives,” *NeuroImage*, vol. 160, pp. 41–54, 2017.
- [5] S. Keilholz *et al.*, “Dynamic properties of functional connectivity in the rodent,” *Brain Connectivity*, vol. 3, no. 1, pp. 31–40, 2013.
- [6] A. Kucyi and K. Davis, “Dynamic functional connectivity of the default mode network tracks daydreaming,” *NeuroImage*, vol. 100, pp. 471–480, 2014.
- [7] E. Allen *et al.*, “Tracking whole-brain connectivity dynamics in the resting state,” *Cerebral Cortex*, vol. 24, no. 3, pp. 663–676, 2014.
- [8] A. Zalesky and M. Breakspear, “Towards a statistical test for functional connectivity dynamics,” *NeuroImage*, vol. 114, pp. 466–470, 2015.
- [9] S. Shakil, C.-H. Lee, and S. Keilholz, “Evaluation of sliding window correlation performance for characterizing dynamic functional connectivity and brain states,” *NeuroImage*, vol. 133, pp. 111–128, 2016.
- [10] R. Hindriks *et al.*, “Can sliding-window correlations reveal dynamic functional connectivity in resting-state fMRI?” *NeuroImage*, vol. 127, pp. 242–256, 2016.
- [11] F. Mokhtari *et al.*, “Sliding window correlation analysis: Modulating window shape for dynamic brain connectivity in resting state,” *NeuroImage*, vol. 189, pp. 655–666, 2019.
- [12] M. Lindquist *et al.*, “Evaluating dynamic bivariate correlations in resting-state fMRI: a comparison study and a new approach,” *NeuroImage*, vol. 101, pp. 531–546, 2014.
- [13] A. Abrol *et al.*, “Replicability of time-varying connectivity patterns in large resting state fMRI samples,” *NeuroImage*, vol. 163, pp. 160–176, 2017.
- [14] D. Handwerker *et al.*, “Periodic changes in fMRI connectivity,” *NeuroImage*, vol. 63, no. 3, pp. 1712–1719, 2012.
- [15] B. Rashid *et al.*, “Dynamic connectivity states estimated from resting fMRI identify differences among schizophrenia, bipolar disorder, and healthy control subjects,” *Frontiers in Human Neuroscience*, vol. 8, p. 897, 2014.
- [16] A. Oppenheim, R. Schafer, and J. Buck, *Discrete-time signal processing*. Upper Saddle River, NJ: Prentice Hall, 1999.
- [17] M. Chung *et al.*, “Cosine series representation of 3d curves and its application to white matter fiber bundles in diffusion tensor imaging,” *Statistics and Its Interface*, vol. 3, pp. 69–80, 2010.
- [18] Z. Yang *et al.*, “Common intrinsic connectivity states among posteromedial cortex subdivisions: Insights from analysis of temporal dynamics,” *NeuroImage*, vol. 93, pp. 124–137, 2014.
- [19] A. Choe *et al.*, “Comparing test-retest reliability of dynamic functional connectivity methods,” *NeuroImage*, vol. 158, pp. 155–175, 2017.
- [20] E. Damaraju *et al.*, “Dynamic functional connectivity analysis reveals transient states of dysconnectivity in schizophrenia,” *NeuroImage: Clinical*, vol. 5, pp. 298–308, 2014.
- [21] P. Barttfeld *et al.*, “Signature of consciousness in the dynamics of resting-state brain activity,” *Proceedings of the National Academy of Sciences*, vol. 112, no. 3, pp. 887–892, 2015.
- [22] B. Rashid *et al.*, “Classification of schizophrenia and bipolar patients using static and dynamic resting-state fMRI brain connectivity,” *NeuroImage*, vol. 134, pp. 645–657, 2016.
- [23] S.-G. Huang *et al.*, “Statistical model for dynamically-changing correlation matrices with application to resting-state brain connectivity,” *arXiv preprint arXiv:1812.10050*, 2018.
- [24] H. Marusak *et al.*, “Dynamic functional connectivity of neurocognitive networks in children,” *Human Brain Mapping*, vol. 38, no. 1, pp. 97–108, 2017.
- [25] J. Su *et al.*, “Heredity characteristics of schizophrenia shown by dynamic functional connectivity analysis of resting-state functional MRI scans of unaffected siblings,” *NeuroReport*, vol. 27, no. 11, pp. 843–848, 2016.
- [26] A. Barber *et al.*, “Dynamic functional connectivity states reflecting psychotic-like experiences,” *Biological Psychiatry*, vol. 3, no. 5, pp. 443–453, 2018.
- [27] M. Jones, “Simple boundary correction for kernel density estimation,” *Statistics and Computing*, vol. 3, no. 3, pp. 135–146, 1993.
- [28] M. Chung *et al.*, “Weighted Fourier representation and its application to quantifying the amount of gray matter,” *IEEE Transactions on Medical Imaging*, vol. 26, pp. 566–581, 2007.
- [29] C. Burghy *et al.*, “Experience-driven differences in childhood cortisol predict affect-relevant brain function and coping in adolescent monozygotic twins,” *Scientific Reports*, vol. 6, p. 37081, 2016.

- [30] N. Tzourio-Mazoyer *et al.*, “Automated anatomical labeling of activations in spm using a macroscopic anatomical parcellation of the MNI MRI single-subject brain,” *NeuroImage*, vol. 15, pp. 273–289, 2002.
- [31] N. Leonardi and D. Van De Ville, “On spurious and real fluctuations of dynamic functional connectivity during rest,” *NeuroImage*, vol. 104, pp. 430–436, 2015.
- [32] W. Shirer *et al.*, “Decoding subject-driven cognitive states with whole-brain connectivity patterns,” *Cerebral Cortex*, vol. 22, no. 1, pp. 158–165, 2012.
- [33] R. Hutchison *et al.*, “Resting-state networks show dynamic functional connectivity in awake humans and anesthetized macaques,” *Human Brain Mapping*, vol. 34, no. 9, pp. 2154–2177, 2013.
- [34] E. Allen *et al.*, “Tracking whole-brain connectivity dynamics in the resting state,” *Cerebral cortex*, vol. 24, pp. 663–676, 2014.
- [35] A. Zalesky *et al.*, “Time-resolved resting-state brain networks,” *Proceedings of the National Academy of Sciences*, p. 201400181, 2014.
- [36] Q. Yu *et al.*, “Assessing dynamic brain graphs of time-varying connectivity in fMRI data: application to healthy controls and patients with schizophrenia,” *NeuroImage*, vol. 107, pp. 345–355, 2015.
- [37] J. Nomi *et al.*, “Dynamic functional network connectivity reveals unique and overlapping profiles of insula subdivisions,” *Human Brain Mapping*, vol. 37, no. 5, pp. 1770–1787, 2016.
- [38] B. Lehmann *et al.*, “Assessing dynamic functional connectivity in heterogeneous samples,” *NeuroImage*, vol. 157, pp. 635–647, 2017.
- [39] A. Choe *et al.*, “Comparing test-retest reliability of dynamic functional connectivity methods,” *NeuroImage*, vol. 158, pp. 155–175, 2017.
- [40] C.-M. Ting *et al.*, “Estimating dynamic connectivity states in fmri using regime-switching factor models,” *IEEE Transactions on Medical Imaging*, vol. 37, no. 4, pp. 1011–1023, 2018.
- [41] A. Baker *et al.*, “Fast transient networks in spontaneous human brain activity,” *Elife*, vol. 3, p. e01867, 2014.
- [42] W. Gilks, S. Richardson, and D. Spiegelhalter, *Markov chain Monte Carlo in practice*. Chapman and Hall/CRC, 1995.
- [43] M. Yaesoubi *et al.*, “Dynamic coherence analysis of resting fMRI data to jointly capture state-based phase, frequency, and time-domain information,” *NeuroImage*, vol. 120, pp. 133–142, 2015.
- [44] H. Ombao *et al.*, “Statistical models for brain signals with properties that evolve across trials,” *NeuroImage*, vol. 180, pp. 609–618, 2018.
- [45] V. Calhoun and T. Adali, “Time-varying brain connectivity in fMRI data: whole-brain data-driven approaches for capturing and characterizing dynamic states,” *IEEE Signal Processing Magazine*, vol. 33, no. 3, pp. 52–66, 2016.
- [46] S. Nielsen *et al.*, “Predictive assessment of models for dynamic functional connectivity,” *NeuroImage*, vol. 171, pp. 116–134, 2018.
- [47] A. Haimovici *et al.*, “On wakefulness fluctuations as a source of BOLD functional connectivity dynamics,” *Scientific Reports*, vol. 7, no. 1, p. 5908, 2017.
- [48] B. Cai *et al.*, “Estimation of dynamic sparse connectivity patterns from resting state fMRI,” *IEEE Transactions on Medical Imaging*, vol. 37, no. 5, pp. 1224–1234, 2018.
- [49] C.-M. Ting *et al.*, “Multi-scale factor analysis of high-dimensional functional connectivity in brain networks,” *IEEE Transactions on Network Science and Engineering*, 2018.
- [50] E. Al-sharoa, M. Al-khassawneh, and S. Aviyente, “Tensor based temporal and multilayer community detection for studying brain dynamics during resting state fMRI,” *IEEE Transactions on Biomedical Engineering*, vol. 66, no. 3, pp. 695–709, 2019.
- [51] R. Salvador *et al.*, “Neurophysiological architecture of functional magnetic resonance images of human brain,” *Cerebral Cortex*, vol. 15, no. 9, pp. 1332–1342, 2005.
- [52] D. Stark *et al.*, “Regional variation in interhemispheric coordination of intrinsic hemodynamic fluctuations,” *Journal of Neuroscience*, vol. 28, no. 51, pp. 13 754–13 764, 2008.
- [53] X.-N. Zuo *et al.*, “Growing together and growing apart: regional and sex differences in the lifespan developmental trajectories of functional homotopy,” *Journal of Neuroscience*, vol. 30, no. 45, pp. 15 034–15 043, 2010.
- [54] J. Anderson *et al.*, “Decreased interhemispheric functional connectivity in autism,” *Cerebral Cortex*, vol. 21, no. 5, pp. 1134–1146, 2010.